



# Deformation of crust and upper mantle in central Tibet caused by the northward subduction and slab tearing of the Indian lithosphere: New evidence based on shear wave splitting measurements

Chenglong Wu<sup>a</sup>, Xiaobo Tian<sup>a,b,\*</sup>, Tao Xu<sup>a,b,\*</sup>, Xiaofeng Liang<sup>a</sup>, Yun Chen<sup>a</sup>, Michael Taylor<sup>c</sup>, José Badal<sup>d</sup>, Zhiming Bai<sup>a</sup>, Yaohui Duan<sup>e</sup>, Guiping Yu<sup>a,f</sup>, Jiwen Teng<sup>a</sup>

<sup>a</sup> State Key Laboratory of Lithospheric Evolution, Institute of Geology and Geophysics, Chinese Academy of Sciences, Beijing 100029, China

<sup>b</sup> CAS Center for Excellence in Tibetan Plateau Earth Sciences, Beijing 100101, China

<sup>c</sup> Department of Geology, University of Kansas, 1735 Jayhawk Boulevard, Lawrence, KS 66045, USA

<sup>d</sup> Physics of the Earth, Sciences B, University of Zaragoza, Pedro Cerbuna 12, Zaragoza 50009, Spain

<sup>e</sup> Earth System Science Programme, Faculty of Science, Chinese University of Hong Kong, Sha Tin, Hong Kong, China

<sup>f</sup> University of Chinese Academy of Sciences, Beijing 100049, China

## ARTICLE INFO

### Article history:

Received 16 November 2018

Received in revised form 25 February 2019

Accepted 28 February 2019

Available online xxxx

Editor: A. Yin

### Keywords:

seismic anisotropy

shear wave splitting

subduction of the Indian lithospheric slab

asthenosphere upwelling

crustal flow

central Tibet

## ABSTRACT

Shear-wave splitting provides insight into geodynamic processes such as lithospheric deformation and upper mantle flow. This study presents shear wave splitting parameters determined from XKS (SKS, SKKS and PKS) and Pms phases (from receiver functions) recorded by the 2D seismic array, SANDWICH, deployed in central Tibet from November 2013 to April 2016. The XKS splitting measurements show a generally strong anisotropy with an average of 1.3 s, that even includes 17 stations with delay times no less than 2.0 s. Interestingly, significantly weak splitting is also observed between Nam Tso and Siling Tso near 90°E. Spatial coherence analysis of the splitting parameters indicates an upper asthenospheric source as the primary cause of seismic anisotropy in the study region. The regionally dominant ENE–WSW oriented upper-mantle anisotropy can emerge from the corner flow in the overlying mantle wedge induced by the subduction of the Indian lithospheric slab. The crustal anisotropy obtained through Pms splitting analysis might reflect lattice preferred orientation of anisotropic minerals formed by the ENE oriented middle-lower crustal flow, with a minor contribution to the strong anisotropy. The weak splitting observations in the east are likely caused by the nearly vertical  $\alpha$ -axis of olivine induced by upwelling asthenosphere at a slab tear in the Indian lithosphere.

© 2019 Elsevier B.V. All rights reserved.

## 1. Introduction

The Tibetan Plateau is the archetype product of continent-continent collision between the Eurasian and Indian plates since ~60 Ma (Yin and Harrison, 2000). Several geodynamic models propose how the high topography of the Tibetan plateau formed and was maintained. These include (1) the lateral eastward extrusion of continental lithosphere along several plateau bounding strike-slip faults (Tapponnier et al., 2001), (2) a thin viscous sheet where the Tibetan Plateau undergoes distributed shortening and crustal thickening (England and McKenzie, 1982), and (3) ductile flow in the middle-lower crust, that decouples deformation between

the upper crust and mantle lithosphere (Clark and Royden, 2000). It is also thought that a series of v-shaped conjugate strike-slip fault systems developed along the Bangong–Nujiang Suture (BNS) accommodates coeval east–west extension and north–south contraction in central Tibet (Taylor et al., 2003; Taylor and Yin, 2009; Yin and Taylor, 2011). Additionally, there is geophysical evidence that the Indian mantle lithosphere is subducting beneath the Asian lithosphere of central Tibet (Li et al., 2008; Kind and Yuan, 2010), and this scenario is different from that of northeastern Tibet where lithospheric deformation is influenced by the far field effects of the India–Eurasia collision. Thus, studying the deformation mechanism of the crust and upper mantle in central Tibet is crucial for understanding processes associated with continental collisions in general, and more specifically the tectonic evolution of the Tibetan Plateau.

Anisotropy causes shear wave splitting (SWS), which has been used to discuss the various tectonic processes associated with

\* Corresponding authors at: State Key Laboratory of Lithospheric Evolution, Institute of Geology and Geophysics, Chinese Academy of Sciences, Beijing 100029, China.

E-mail addresses: [txb@mail.iggcas.ac.cn](mailto:txb@mail.iggcas.ac.cn) (X. Tian), [xutao@mail.iggcas.ac.cn](mailto:xutao@mail.iggcas.ac.cn) (T. Xu).

the crust and mantle (Silver, 1996; Savage, 1999). Previous research supports the idea that seismic anisotropy in the upper crust is mostly associated with stress-aligned fluid-saturated cracks (Crampin and Peacock, 2005); and that anisotropy in the lower continental crust originates primarily from lattice preferred orientation (LPO) of anisotropic minerals induced by plastic flow (Tatham et al., 2008). At deeper levels, anisotropy in the upper mantle results from strain-induced LPO of intrinsically anisotropic mantle minerals, such as olivine (Zhang and Karato, 1995). SWS of core-mantle boundary P-to-S converted phases, including SKS, SKKS and PKS collectively called XKS phases, provides an ideal tool for exploring mantle anisotropy below the seismic receiver due to the steep angle of incidence of XKS arrivals. Splitting parameters include the polarization orientation of the fast wave ( $\varphi$ ), which measures the orientation of the anisotropy, and the delay time or splitting time between the fast and slow waves ( $\delta t$ ), which indicates the strength of the anisotropy integrated from the core-mantle boundary (CMB) to the surface along the ray path. Unlike the XKS phases converted at the CMB, the Moho P-to-S phase (Pms) is converted from a near vertically incident P-wave at the crust-mantle boundary, therefore, the source of the anisotropy must occur above the Moho. Thus the Pms splitting provides an ideal means to isolate crustal anisotropy from that of the mantle, as well as characterizes the nature of crustal deformation.

SWS results have been widely used to discuss the relationship between the Indian and Tibetan lithosphere beneath the plateau (Sandvol et al., 1997; Chen and Ozalaybey, 1998; Huang et al., 2000; Fu et al., 2008; Chen et al., 2010; Zhao et al., 2014). Assuming that the Indian lithosphere has very weak anisotropy, the observation of strong SWS in southern Tibet has been suggested as the leading edge of the Indian lithosphere and deforming Eurasian lithospheric mantle (Chen and Ozalaybey, 1998; Huang et al., 2000; Chen et al., 2010; Zhao et al., 2014). However, this interpretation has been challenged since there is significant SWS observed in Indian plate (Kumar and Singh, 2008). Within the scope of this controversy, the null or weak SWS observations in southern Tibet have been interpreted as subvertical mantle shear strain resulting from downwelling mantle flow of the thickened Indian lower continental lithosphere (Sandvol et al., 1997), or possibly the subvertical subduction of Indian lithosphere located just south of the BNS (Fu et al., 2008). Additionally, the variation of SWS measurements along an east-trending profile has been interpreted as slab tearing of subducting Indian lithosphere (Chen et al., 2015). Nevertheless, a better understanding about the source of the anisotropy is needed to reconcile these results, either from the fabric of deforming/deformed lithospheric mantle or the asthenospheric flow associated with plate motions. Additionally, the contribution of crustal anisotropy of Tibet to SWS observations should be considered because of Tibet's remarkable crust thickness (McNamara et al., 1994), let alone the existence of the middle-lower crustal flow proposed by many studies (Clark and Royden, 2000; Sherrington et al., 2004; Wu et al., 2015).

The current SWS measurements in Tibet are mostly along different survey profiles, while in this study, we conducted SWS measurements of XKS and Pms waves utilizing the 2D broadband seismic station array SANDWICH (Liang et al., 2016a) operated by the Institute of Geology and Geophysics, Chinese Academy of Sciences (IGGCAS), over a two-year span, allowing us to track the 2D lateral variations of SWS and related crust and upper mantle deformation.

## 2. Data and methods

The SANDWICH experiment is a 2D broadband seismic network in central Tibet spanning both sides of the BNS, from the northern Lhasa block to the southern Qiangtang block (Fig. 1). The network

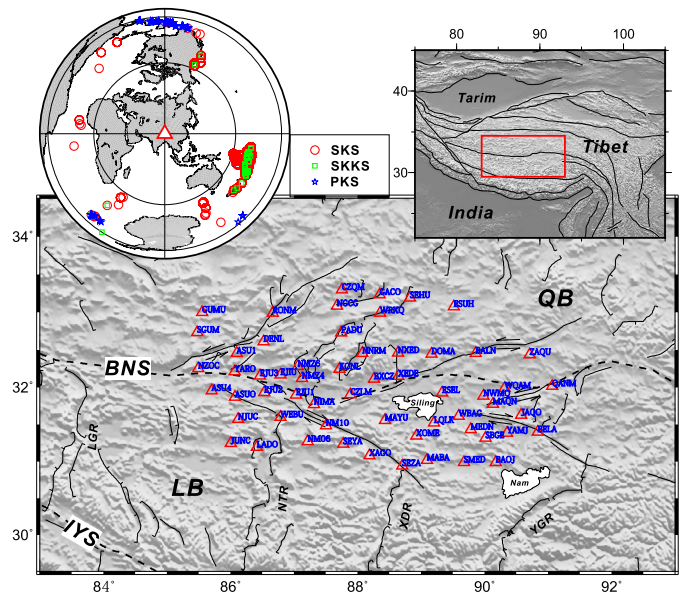


**Fig. 1.** Shaded topographic map where the main tectonic features in the central area of Tibet and the location of the SANDWICH seismic array are shown. The study area is contoured by a red rectangle in the top right inset. The red triangles indicate the geographical positions of the seismic stations. The blank areas represent large lakes. The teleseismic events used for XKS splitting measurements are shown on a world map in the top left inset. The red triangle in the center of the circle marks the location of the seismic array. The two concentric circles mark epicentral distances of 85° and 140° from the study region. The red circles, green squares and blue stars indicate the events that generate the SKS, SKKS and PKS phases used in this study, respectively. Abbreviations: LB, Lhasa block; QB, Qiangtang block; IYS, Indus-Yarlung suture; BNS, Bangong-Nujiang suture; LGR, Longgar rift; NTR, Nyima-Tingri rift; XDR, Xainza-Dingjye rift; YGR, Yadong-Gulu rift; Nam, Nam Tso; Siling, Siling Tso. (For interpretation of the colors in the figure(s), the reader is referred to the web version of this article.)

operated from November 2013 to April 2016 and includes 58 seismographs with an average station spacing of 40 km. Each station was equipped with a Güralp CMG-3ESP three-component sensor of 50 Hz–30/60 s and a RefTek 72A-8/130-1 digital recorder (Liang et al., 2016a).

### 2.1. XKS splitting measurements

Earthquakes with magnitude  $\geq 5.5$  and epicentral distances ranging from 85° to 140° were selected for analysis. A total of 176 events with broad azimuthal coverage is analyzed in this study (Fig. 1). We used teleseismic SKS, SKKS and PKS phases to measure SWS under each receiver. Most of the measurements were band-pass filtered to 0.04–0.5 Hz, because it was found to be the most effective frequency band to increase the signal-to-noise ratio and so get better waveforms (Gao et al., 2010); only some measurements were filtered to 0.03–0.2 Hz, which also includes the primary energy of XKS. We performed SWS analysis with the help of SplitLab (Wüstefeld et al., 2008). The rotation cross-correlation (RC) method (Bowman and Ando, 1987) and the transverse-component minimization (SC) method (Silver and Chan, 1991) were used simultaneously in a grid-research of the splitting parameters  $\varphi$  (fast wave polarization direction) and  $\delta t$  (delay time) to best remove the splitting effect. Reliability is ensured when similar results are obtained from both methods. For each event, we calculated XKS splitting over multiple time windows and chose the one with the smallest error. Fig. 2 is an example of results we obtained using the SplitLab package. It shows well the splitting measurement of SKS phases generated by the 2015:167:06:17 event and recorded at SEHU station (Figs. 2a–k). Similar splitting parameters were obtained using both the RC and SC methods. The effect of

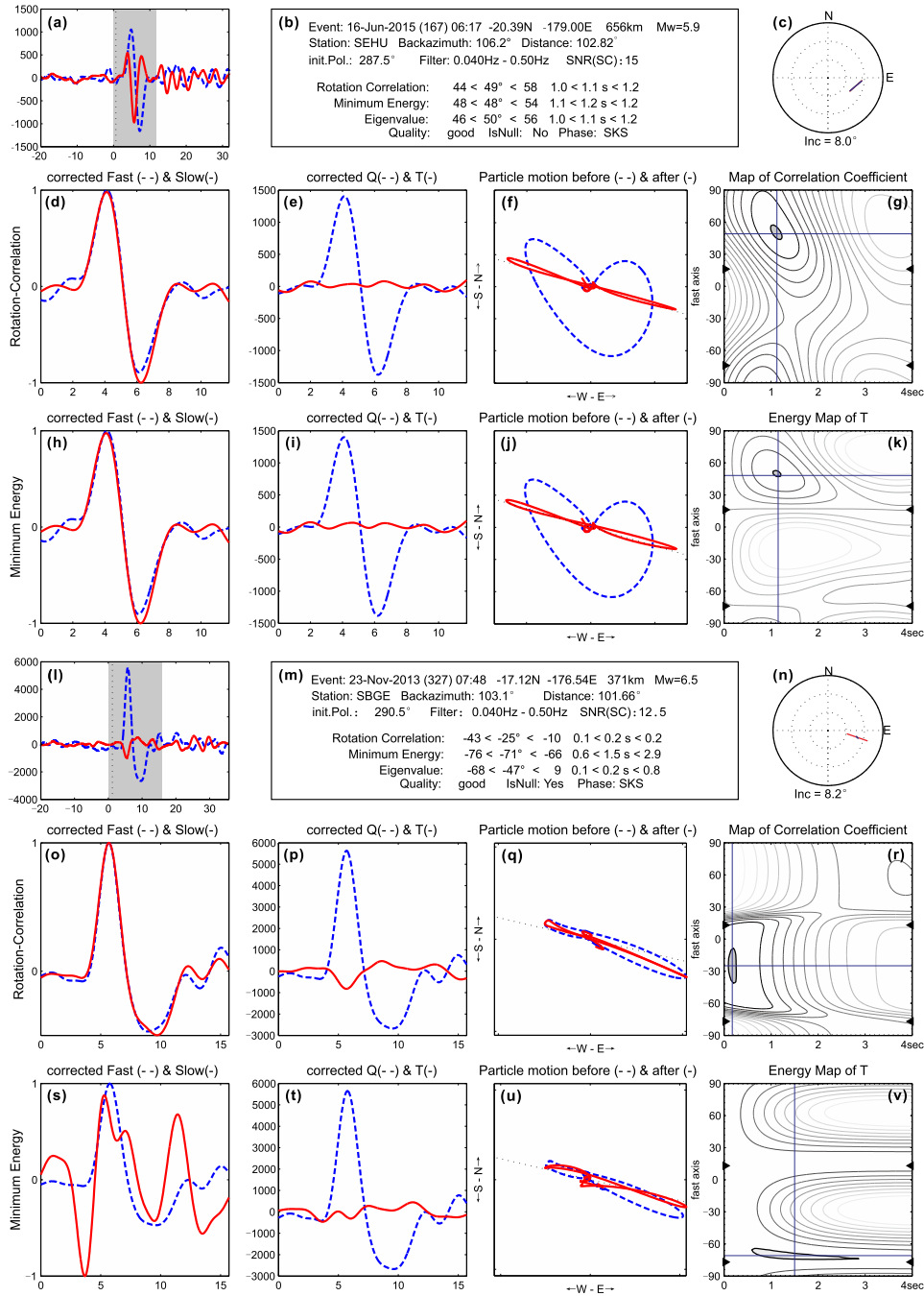


**Fig. 2.** Example of SKS splitting measurement using the SplitLab software package (Wüstefeld et al., 2008) for the event 2015:167:06:17 recorded at SEHU station. Upper panels (a-c) display: (a) the initial seismograms; (b) information about the event-station pair and the measurement result; (c) the stereoplot centered at SEHU station. Middle panels (d-g) display: (d) the result of the rotation-correlation (RC) technique and the seismogram components in the fast (blue dashed line) and slow (red continuous line) polarization directions for the RC-anisotropy system after RC-delay correction (normalized); (e) radial Q (blue dashed line) and transverse T (red continuous line) components after RC-correction (not normalized); (f) particle motion before (blue dashed line) and after (red continuous line) of the RC-correction; (g) map of correlation coefficients depending on the possible pairs of fast polarization direction and delay time. Lower panels (h-k) display the results of applying the minimum energy (SC) technique that are very similar to the previous ones. The graphics (l-v) are another example of SKS splitting measurement for the event 2013:327:07:48 recorded at SBGE station (same legend as for the above plots), with the peculiarity that it is a null case.

the anisotropy is removed typically with similar waveforms between fast and slow waves, with little energy on the transverse component, and the linearized polarization of the initially elliptical particle motion after the anisotropy correction. Null measurements may occur if the wave propagates through an isotropic (or weakly anisotropic) medium, or if the initial polarization coincides with either the fast or the slow axis (Savage, 1999), which can be distinguished by comparing the results obtained from the RC and SC methods (Wüstefeld and Bokelmann, 2007). An example is shown

for the 2013:327:07:48 event recorded at station SBGE (Figs. 2l-v). Note that the energy is mostly restricted to the radial component and is invisible on the transverse component.

Quality of the SWS measurements is evaluated by the differences between the results given by the RC and SC techniques, i.e. through the angular difference in  $\varphi$  ( $\Psi = |\varphi_{RC} - \varphi_{SC}|$ ) and the ratio of  $\delta t$  ( $\rho = \delta t_{RC} / \delta t_{SC}$ ) (Wüstefeld and Bokelmann, 2007). “Good” splitting measurements are defined if  $0.8 \leq \rho \leq 1.1$  and  $\Psi \leq 10^\circ$  and ‘fair’ if  $0.7 \leq \rho \leq 1.2$  and  $\Psi \leq 15^\circ$ . Null measurements are

defined as ‘good’ when  $35^\circ \leq \Psi \leq 55^\circ$  and  $\rho \leq 0.2$ . Any remaining measurements outside of these values are considered “poor”. We attempt to avoid misinterpretations due to poor quality data, by only using ‘good’ and ‘fair’ measurements for our analysis. Stable results over a broader range of analysis occurred using the SC method, thus splitting measurements using this method will be presented. Results obtained using the RC method are considered for determining the rank in quality. To improve the reliability of splitting measurements, several more criteria are needed with the SC method: (1) signal-to-noise ratio (SNR)  $\geq 4$  (as defined in Splitlab); (2) the back-azimuth separation from the fast or slow polarization directions  $|\Delta\text{BAZ}|$  must be above  $15^\circ$ , since the results given by the SC method with  $|\Delta\text{BAZ}|$  below  $10^\circ$  are unstable; and (3) the uncertainties of the fast wave polarization direction  $\varphi$  and delay time  $\delta t$  must be less than  $22.5^\circ$  and 0.5 s, respectively.

## 2.2. Depth of anisotropy

Because of the steep incidence of the XKS ray paths, XKS splitting observations have good lateral resolution (compared to other anisotropy-measuring technique) but little vertical resolution. The most widely used approach to estimate the anisotropy depth, the center depth of the anisotropic layer, is the intersecting Fresnel-zone approach (Alsina and Snieder, 1995). However, this approach is limited to situations in which events from opposite directions are available, and there is significant lateral variation of SWS between nearby stations simultaneously.

In this study, we applied a more generalized extension of the intersecting Fresnel-zone approach based on the spatial coherency of splitting parameters (Liu and Gao, 2011). The optimal anisotropy depth was searched in the 0–350 km range to reach the highest spatial coherency of the observed splitting parameters. The incremental interval for the assumed depths is 5 km. For each depth, the study area is divided into overlapping blocks with an area of  $dx \times dx$  square-degrees. The variation factors at this depth,  $F_{\delta t}$  for  $\delta t$  and  $F_\varphi$  for  $\varphi$ , are average values of standard deviation for each block. The variation factor,  $F_v$ , is computed as a dimensionless weighted average of  $F_\varphi$  and  $F_{\delta t}$ . They are calculated using equations (4)–(7) in Liu and Gao (2011). The block size is important to keep the reliability of the depth search procedure. When the block size  $dx$  is too small (for example  $0.05^\circ$ ), there are typically about two measurements for each block, which will lead to an unstable  $F_v$  depth determination with exceedingly large uncertainties. When  $dx$  is too large (for example  $0.4^\circ$ ), the measurements inside each block may not be spatially consistent, which will lead to a broad  $F_v$  curve and reduced peak-to-peak amplitude (Liu and Gao, 2011). In this study, different  $dx$  test values from  $0.16^\circ$  to  $0.28^\circ$  with an interval of  $0.04^\circ$  were utilized to generate the  $F_v$  curves (Fig. 3). To avoid the unstable variation,  $F_v$  was smoothed based on 11 adjacent values. The depth corresponding to the minimum variation factor on the resulting  $F_v$  curves suggests that the optimal depth for the center of the anisotropic layer lies approximately between 145 km and 155 km, with an average of 150 km (Fig. 3).

## 2.3. Crustal anisotropy

To isolate the crustal contribution to the observed SWS of XKS phases, we used the azimuthal arrival variations of the Moho converted Pms-wave to estimate the crustal anisotropy (in addition to XKS splitting). We selected seismic waveforms of earthquakes with magnitude  $\geq 5.3$ , at epicentral distances between  $30^\circ$  to  $90^\circ$ . We filtered the data at 0.03–2.0 Hz frequency band and computed radial receiver functions in the time domain. Measuring splitting parameters from an individual receiver function can introduce large errors due to the limited SNR (Liu and Niu, 2012), so we chose to

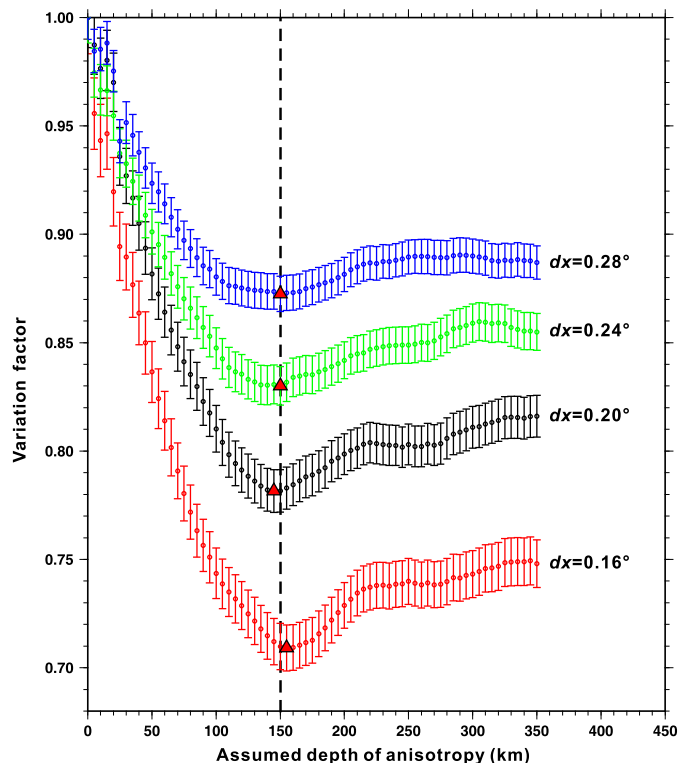


**Fig. 3.** Spatial coherence analysis based on XKS splitting. The aim of this analysis is to determine the optimal anisotropy depth. The results for places within the so-called Weak Area (see Fig. 4) were not considered for analysis. The procedure is clearly described in the section 2.2. Vertical bars mean uncertainties. The red triangles mark the estimated anisotropy depth corresponding to the minimum variation factor for different block sizes. The optimal anisotropy depth reaches about 150 km (vertical dashed line).

fit pair of parameters ( $\varphi$  and  $\delta t$ ) for all the receiver functions at a single station.

A simple and weakly anisotropic crust will lead to azimuthal variations of the Pms arrival times, so a pair of splitting parameters can be estimated by fitting a cosine function for the Pms arrivals at different back-azimuth (Liu and Niu, 2012):

$$t_{pms} = t_0 - \frac{\delta t_c}{2} \cos[2(\alpha - \varphi_c)]$$

where  $t_0$  denotes the Pms arrival times in the isotropic case,  $\delta t_c$  is the delay time associated to the crustal anisotropy,  $\alpha$  is the back-azimuth of the receiver function, and  $\varphi_c$  is the fast polarization orientation. The splitting parameters associated with the crustal anisotropy is obtained through a grid-research of the combination of  $t_0$ ,  $\varphi_c$  and  $\delta t_c$  that gives the maximum amplitude of the stacked radial receiver functions. We searched  $t_0$  in the 5–12 s range with an increment of 0.1 s and  $\varphi_c$  in the  $0$ – $180^\circ$  range with  $1^\circ$  increments. Considering the thickness and history of crustal deformation in the study area, the search range of  $\delta t_c$  was set to 0.0–1.5 s with a step of 0.05 s. Receiver functions were averaged in  $10^\circ$  bins in order to prevent dominant weighting from a certain back-azimuth due to the uneven earthquake distribution.

For reliable results, several requirements need to be satisfied (Wu et al., 2015). First, there is a single layer of crustal anisotropy with a horizontal symmetrical axis beneath the reference station. Second, the azimuthal coverage must be sufficient to obtain a pair of reliable splitting parameters by fitting the azimuthal variations of the Pms arrival times, requiring a long-duration recording, a stable performance of the station, and a suitable location of the station relative to the major seismic belts. Finally, a sufficiently sharp and smooth Moho will generate clearer Pms arrivals.

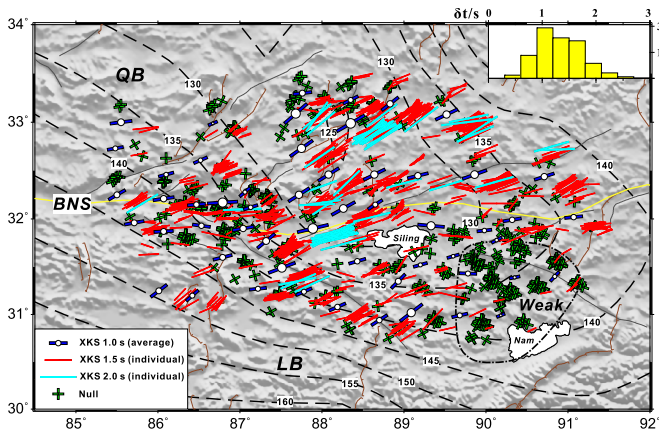


**Fig. 4.** Individual and averaged XKS splitting measurements: fast wave polarization direction and delay time. Individual measurements are projected to their piercing points at 141 km depth. Red bars represent XKS splitting measurements for delay time smaller than 2.0 s; light blue bars show the results for delay time above 2.0 s; dark blue bars represent station-averaged splitting measurements, while green crosses indicate fast and slow polarization directions corresponding to null cases. The bottom left inset shows the scales for delay times. The histogram in the upper right box illustrates the distribution of delay times (in seconds). The area bounded by a dash line in the lower right quadrant scarcely shows anisotropy and is called Weak Area. Dashed contour lines give the thickness (in km) of the Tibetan lithosphere (Zhang et al., 2014). Acronyms: LB, Lhasa block; QB, Qiangtang block; BNS, Bangong-Nujiang suture.

### 3. Results

#### 3.1. Spatial distribution of XKS splitting parameters

Using the above criteria, we obtain 1020 total splitting measurements (including 824 good and 196 fair ones) and 633 reliable null measurements. The weighted average of the splitting parameters ( $\varphi$  and  $\delta t$ ) for each station is calculated based on the respective standard deviations (Table S1, Figs. S1 and S2). There are no systematic azimuthal variations in the observed splitting parameters (individual measurements projected to 141 km depth piercing points), suggesting a single anisotropic layer with a horizontal symmetrical axis or multiple layers with similar fast wave polarization directions explain the SWS parameters (Fig. 4).

The results reveal a complex spatial variation of the XKS splitting parameters: strong anisotropy observed throughout the study, with an exception of weak anisotropy in the southeast part of the region labeled in Fig. 4 as a “Weak Area”. Numerous significant splitting measurements are observed throughout the study area –  $\varphi$  is aligned mainly in ENE-WSW direction despite some nearly E-W observations. The average value of  $\delta t$  is 1.3 s with individual splitting measurements greater than 2.0 s at 17 stations (in Fig. 4 the light blue bars represent splitting measurements with  $\delta t \geq 2.0$  s), which is twice the global average of 1.0 s (Silver, 1996). An abrupt change of  $\delta t$  occurs in the southeast part of the study area between Nam Tso and Siling Tso. There are more than 200 null measurements with large back-azimuthal coverage in this area, except locally weak splitting measurements. Therefore, it indicates isotropy or a very weak anisotropy weaker than our detection threshold (i.e., “Weak Area” in Fig. 4).

The SWS measurements agree well with previous results (Fig. 5) (Huang et al., 2000; Chen et al., 2010; Zhao et al., 2014; Chen et al., 2015). It is noteworthy that the Weak Area of SWS strength is confirmed by measurements along the INDEPTH III profile (Huang et al., 2000), and the small average delay time (about 0.3 s, usually defined as null measurement) between the Xainza-Dingjye rift (XDR) and the Yadong-Gulu rift (YGR) (Chen et al., 2015). Furthermore, the boundary where the strong anisotropy becomes weak is located near 89.7°E and 31.8°N (Fig. 4).

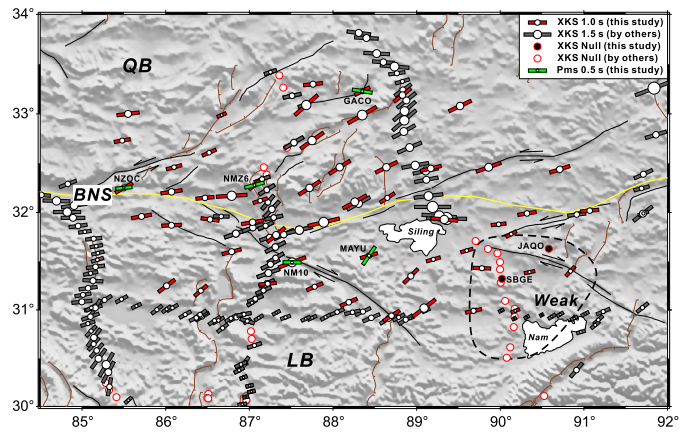


**Fig. 5.** Comparison of the station-averaged XKS splitting measurements (red bars) with SWS parameters (gray bars) obtained by previous studies (McNamara et al., 1994; Sandvol et al., 1997; Huang et al., 2000; Chen et al., 2010; Zhao et al., 2014; Chen et al., 2015) and the Pms splitting parameters (green bars) obtained through radial receiver functions in this study. The upper right inset shows the scales for delay times. Note that the scales for Pms and XKS splitting times are different for comparison. Red circles represent null cases in previous studies that are mostly concentrated in the Weak Area (contoured by the dash line). Black dots are null cases in this study. Acronyms: LB, Lhasa block; QB, Qiangtang block; BNS, Bangong-Nujiang suture.

#### 3.2. Crustal anisotropy based on Pms splitting

Careful visual inspection of all the receiver functions finds that 6 of the 58 stations satisfy the requirements mentioned in section 2.3. The crustal anisotropy is estimated using Pms arrival times recorded by stations GACO, NZOC, NMZ6, NM10, MAYU and JAQO (Fig. 6). The delay times vary from 0.45 s to 0.60 s with an average of 0.53 s, which are slightly larger than those from McNamara et al. (1994) in northern Tibet. Exceptions include the splitting parameters 135° and 0.1 s for station JAQO. The fast wave polarization directions range between 34° and 99° with an average value of 76°, consistent with a middle to lower crustal anisotropy with a fast polarization aligned ENE at stations AMDO and WNDO stations by fitting the radial and transverse receiver functions (Sherrington et al., 2004). A comparison shows that the fast polarization directions of the split Pms-wave are roughly parallel to the XKS splitting measurements with an angular difference within 40° (Fig. 5). The delay times ( $\sim 0.5$  s) indicate that the crustal anisotropy is a small proportion of the large anisotropy obtained by XKS splitting.

### 4. Discussion

#### 4.1. Anisotropy in the upper mantle

We suggest that the observed SWS comes mainly from the LPO of olivine developed in the upper asthenosphere rather than the lithosphere, although contribution of the lithosphere to the observed anisotropy cannot be ruled out based on the following: (1) there is a large angular difference between the fast polarization directions and the surface geology in central Tibet (e.g., the active v-shaped conjugate strike-slip faults); (2) the fast polarization directions are aligned ENE-WSW without significant changes across the terrane boundary (BNS) (Fig. 4); (3) the estimated center depth of the anisotropic layer (150 km) is located at greater depth than the lower limit of the relatively thin lithosphere as revealed by surface wave tomography (Zhang et al., 2014), which is consistent with a low Pn-wave velocity and inefficient high-frequency Sn-wave propagation (Liang and Song, 2006); (4) large splitting times are observed in areas of thin lithosphere ( $\sim 88^\circ$ E along the BNS).

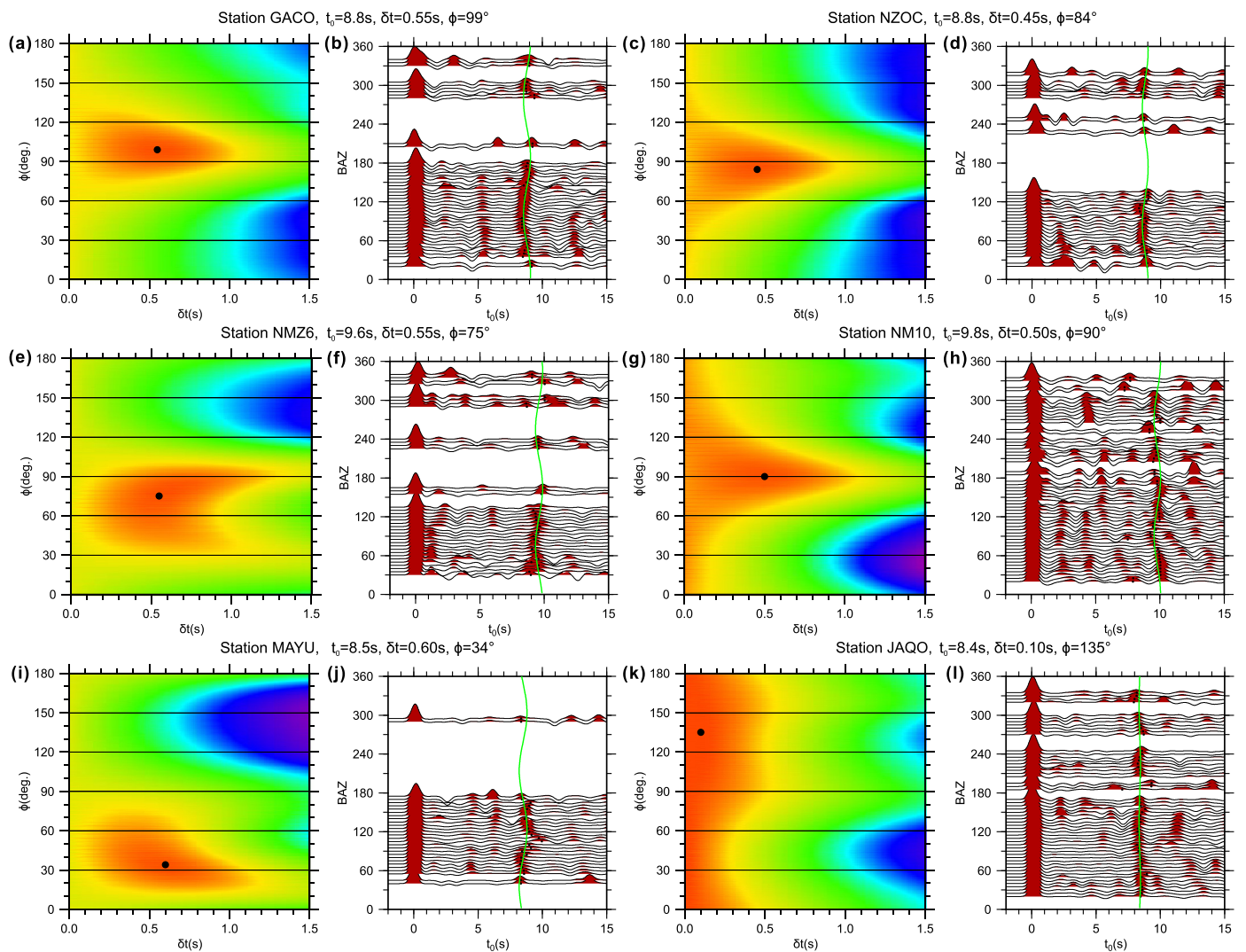


**Fig. 6.** Measurements of crustal anisotropy using Pms wave arrival times recorded by stations GACO (a-b), NZOC (c-d), NMZ6 (e-f), NM10 (g-h), MAYU (i-j) and JAQO (k-l). The color diagrams on the left of each plot show the stacking amplitudes calculated as a function of all candidate pairs of fast polarization directions and delay times. The black points mark the locations of the peak amplitudes in each case, i.e. the optimal pair of splitting parameters. The corresponding values of the Pms arrival time ( $t_0$ ), delay time associated to the anisotropy of the crust ( $\delta t$ ) and fast polarization direction ( $\phi$ ) are included on the top of each plot. The traces of the radial receiver functions are plotted against the back-azimuth (BAZ) on the right of each stacking amplitudes map. The green curve represents the theoretical Pms moveout estimated by the cosine function (section 2.3) using the optimal pair of splitting parameters.

The average fast polarization direction of  $65^\circ$  in the study area (with exception of the Weak Area) is close to the APM direction of the Indian plate at about  $50^\circ$  (Fig. 7). This implies that the source of the anisotropy may be related to the leading edge of subducting Indian lithosphere (Liang et al., 2016b) (Fig. 8). The downward motion of the Indian lithospheric slab induces an ENE oriented corner flow in the overlying mantle wedge, which is roughly parallel to the APM of the Indian plate, generating the observed anisotropy. Various seismic imaging techniques, including receiver functions (Zhao et al., 2010), body wave tomography (Li et al., 2008; Liang et al., 2016b) and surface wave tomography (Li et al., 2013), indicate that from west to east the horizontal subducting distance of the Indian lithosphere under the Tibet varies laterally (Kind and Yuan, 2010), as well as the dip angle of subducting Indian lithosphere (Li et al., 2008). The complex structure of the Indian lithospheric slab front may result in the highly varying splitting parameters (Chen et al., 2015).

#### 4.2. Anisotropy in the crust

The fast directions for stations NZOC, NMZ6, NM10, MAYU correlate well with the approximate surface trace of the Bangong-Nujiang suture zone, which was reactivated during Cenozoic crustal shortening (Yin and Harrison, 2000). The anisotropy at these stations may be related to the north dipping Oligocene-Miocene Shiquanhe-Gaize-Amdo thrust system (Yin and Harrison, 2000; Kapp et al., 2003, 2005; Yin, 2010). It is estimated that the upper crust in the Nima area underwent  $>59$  km of shortening from Cretaceous to mid-Tertiary time (Kapp et al., 2007). During this shortening phase, the sedimentary rocks should have thickened, and at lower structural levels experienced greenschist facies metamorphism, foliation development (i.e., anisotropic fabric) due to increasing temperature and pressure conditions. Greenschist rocks are observed in the metasedimentary-matrix mélangé in the Nima area (Kapp et al., 2007), which may also contribute to the anisotropy observed at stations NMZ6 and NM10. Station GACO is located up plunge of the Qiangtang anticlinorium fold axis that is

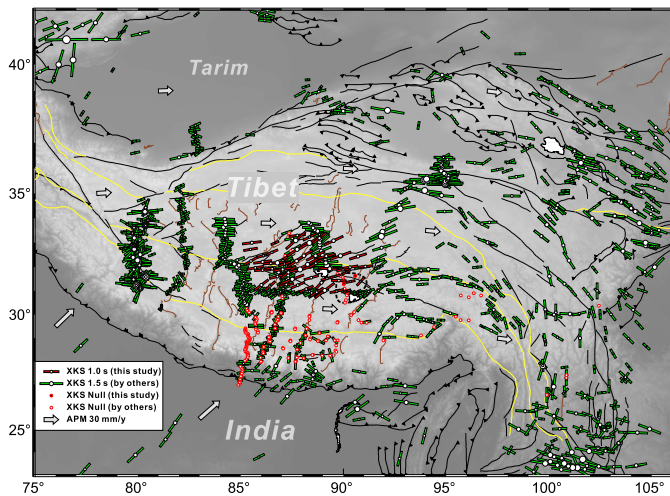


**Fig. 7.** SWS measurements obtained in this study (red bars) along with others obtained by previous studies in the wider framework of the Tibetan Plateau (green bars). The results can be found in the following link: <http://splitting.gm.univ-montp2.fr/>. Red circles represent null cases in previous studies. Black dots are null cases in this study. The small area contoured by the dash line is the Weak Area in this study. White arrows indicate the Absolute Plate Motions (APM) calculated by the Plate Motion Calculator (<http://www.unavco.org>) using the GSRM V2.1 model (Kreemer et al., 2014). The Indian slab is moving toward N50°E in a no-net-rotation frame.

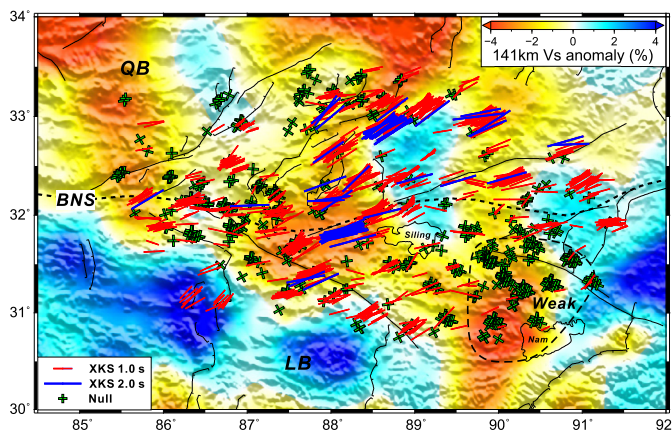


**Fig. 8.** XKS splitting measurements on a shear-wave velocity map obtained using body-wave finite-frequency tomography (Liang et al., 2016b). The base map shows the distribution of shear-wave velocity anomalies at 141 km depth (see color scale in the upper right inset). Different color bars show individual SWS measurements projected to piercing points at 141 km depth. Red bars represent splitting results for delay time smaller than 2.0 s; dark blue bars show the results for delay time above 2.0 s, while green crosses indicate fast and slow polarization directions corresponding to null cases. The bottom left inset shows the scales for delay times. The area contoured by the dash line is the Weak Area in this study. Acronyms: LB, Lhasa block; QB, Qiangtang block; BNS, Bangong-Nujiang suture.

cut by north-trending rifts (Kapp et al., 2000, 2003). The anisotropy observed at GACO may be related to younger east-directed extensional systems. Nevertheless, splitting times in the upper crust are generally no more than 0.2 s (Savage, 1999), occupying the upper half of the central Tibetan crust. Thus, we infer the crustal anisotropy is dominantly from the middle-lower crust.

The localized low  $V_s$  regions (Rapine et al., 2003), high conductivity zones (Solon et al., 2005), and the absence of seismicity deeper than 30 km (Zhu et al., 2017) point to a ductile and even partially melted middle-lower crust, which is also supported by the strong crustal attenuation of the nearby regions (Zhao et al., 2013). Thus we speculate that there exists more plausibly ongoing flow in middle-lower crust, inducing the mineral LPO and seismic anisotropy we observed. For a 40-km-thick middle-lower crustal

layer, the observed splitting time requires an anisotropy of approximately 5%. This high degree of anisotropy is reported for amphibolite rocks (a strongly anisotropic mineral). Tatham et al. (2008) found that fabrics in amphibolite rocks are primarily deformation fabrics and can generate up to 13% seismic anisotropy under strong shear. Thus the observed 5% anisotropy may originate from LPO of amphibolite minerals related to middle-lower crustal flow.

The crustal anisotropy observed at station JAQO is weak, broadly consistent with an isotropic medium. While the apparent lack of anisotropy could be due to the lack of a coherent LPO fabric, dipping axis of symmetry, or multiple layers with variably oriented anisotropy, a viable mechanism explaining this observation requires more detailed research.

#### 4.3. Asthenosphere upwelling in the Weak Area

There is a remarkable variation of seismic anisotropy for the SANDWICH seismic array observed by XKS, between Nam Tso and Siling Tso (Fig. 4). The results show an abrupt change from strong to weak anisotropy, suggesting a substantial lateral variation of the underlying structure. There are two sets of possible mechanisms to explain the null or weak splitting measurements beneath southern Tibet: (1) the nearly vertical  $\alpha$ -axis of olivine associated with a subvertical flow either from the thickened downwelling Indian lower lithosphere (Sandvol et al., 1997), or from a vertical asthenospheric flow resulting from the subvertical subduction of the Indian lithosphere (Fu et al., 2008); (2) the lack of a coherent LPO fabric in the Indian lithosphere beneath southern Tibet (Chen and Ozalaybey, 1998; Huang et al., 2000; Chen et al., 2010). However, obvious splitting (about 1.0 s) and fast polarization directions close to the APM-related strain in the Indian Shield have been obtained (Kumar and Singh, 2008). Thus, we prefer the hypothesis that the  $\alpha$ -axis of olivine is near vertical to explain the null or weak SWS observations.

Based on the spacing and stability analysis of the north-trending rifts, and the age of rift initiation, Yin (2000) suggest that subducting Indian mantle lithosphere beneath southern Tibet is involved in east-west extension of Tibet. Subsequent studies also interpret that Indian mantle lithosphere may be torn (Hou et al., 2006). A more recent body-wave finite-frequency tomography (Liang et al., 2016b) suggests that a north-trending low-velocity anomaly in the uppermost mantle near 90°E is a tear in the Indian lithospheric slab with upwelling asthenosphere – located approximately in the same region where we detect weak anisotropy (Fig. 8). We suggest the most likely explanation for the weak anisotropy is the upwelling asthenosphere that results in a nearly vertical  $\alpha$ -axis of olivine (Fig. 9). Other studies suggest similar asthenosphere upwelling in this area. For example, in the frame of an extensional mechanism and reduced seismic velocity in the upper mantle, the Moho uplift suggests upwelling asthenosphere, coincident with our results (Tian et al., 2015). Slab-tearing and asthenosphere upwelling have also been proposed based on the lateral variation of SWS measurements (Chen et al., 2015). Significantly weak anisotropy is also observed in some other places associated with lithospheric extension and upwelling asthenosphere (e.g., Xue and Allen, 2005).

A lot of null splitting measurements have been recognized in previous studies south of  $\sim 30^\circ\text{N}$  (Fig. 7), which might be regarded as the boundary to separate the weak anisotropy region (Indian realm) and the strong anisotropy region (Asian/Tibetan realm). The cause of such a large-scale region of weak anisotropy may be different from that prevailing in our study area. It is conceivable that anisotropy caused by the inclining asthenospheric flow should be smaller than the one from the horizontal flow. At the same time, the strong deformation of the bending Indian lithosphere beneath

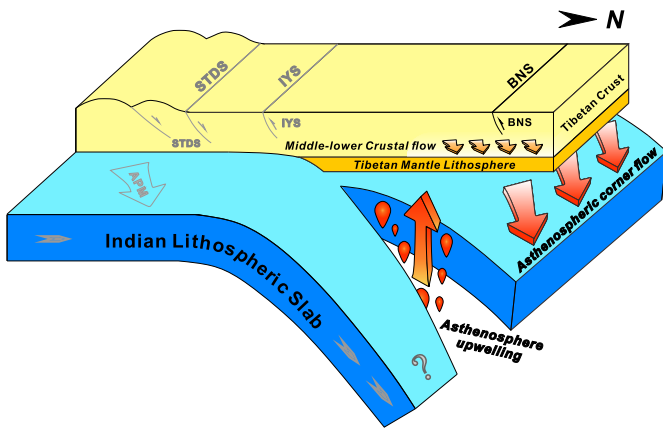


**Fig. 9.** Cartoon to help the interpretation of the anisotropy of the crust and upper mantle in central Tibet influenced by the subduction of the Indian lithospheric slab. Acronyms: STDS, Southern Tibetan Detachment System; IYS, Indus-Yarlung suture; BNS, Bangong-Nujiang suture. The light blue arrow indicates the Absolute Plate Motion (APM) of the Indian slab which is moving toward N50°E in a no-net-rotation frame. The strong anisotropy comes from the combined effect of the middle-lower crustal flow and the corner flow in the overlying mantle wedge induced by the downward motion of the Indian lithospheric slab with roughly parallel fast polarization directions. The weak anisotropy in the area between Nam Tso and Siling Tso is caused by the asthenosphere upwelling through a slab tear in the subducting Indian lithosphere.

Tibet might result in a distinct anisotropy. However, the fast polarization directions in the subducting Indian lithosphere and in the underlying asthenosphere might differ in a significant angle, which causes the weak anisotropy south of 30°N. Then the observed change of anisotropy intensity around 30°N may represent a mantle trench between the Indian and Tibetan mantle lithosphere (Chen et al., 2010), and the strong anisotropy exists in the mantle wedge north of the Indian lithosphere.

## 5. Conclusions

We use 2D broadband seismic data recorded in central Tibet to carry out XKS and Pms (receiver functions) splitting analyses to investigate the deformation style of the crust and upper mantle. The first-order pattern of XKS splitting measurements shows a strong overall anisotropy with delay times larger than 2.0 s at 17 stations, and a local observation of weak anisotropy between Nam Tso and Siling Tso. Spatial coherence analysis of the XKS splitting parameters determines the central depth of the anisotropic layer at ~150 km, indicating that the observed anisotropy comes mainly from the LPO of olivine in the upper asthenosphere. The SWS measurements show a dominant ENE-WSW orientation that may come from the corner flow in the overlying mantle wedge induced by the downward motion of the Indian lithospheric slab. Crustal seismic anisotropy contributes little to the strong anisotropy observed in the region, and may originate from the mineral LPO induced by ENE directed middle-lower crustal flow. The observed weak anisotropy is likely due to the nearly vertical  $\alpha$ -axis of olivine, as a consequence of asthenosphere upwelling through a slab tear in the subducting Indian lithosphere (Fig. 9).

## Acknowledgements

This paper is dedicated to the memory of Prof. Zhongjie Zhang (1964–2013). We thank the Seismic Array Laboratory, IGGCAS, for the preparation and maintenance of the recording instruments. We appreciate the assistance of the members of the SANDWICH field team, who collected the data used in this study, including Drs. Wei Li, Minghui Zhang, Xi Guo, Beibei Zhou, Shitan Nie, Gaochun Wang, Zhen Liu, Zhenbo Wu, Minling Wang, Ping Tan and Xiaopeng

Zhou. We also thank Profs. Fuqin Zhang and Laicheng Miao, Drs. Youqiang Yu and Sicheng Zuo for their contributions to valuable discussions. Helpful comments and suggestions from Prof. Stephen S. Gao and another anonymous reviewer improved the presentation of this paper. We gratefully acknowledge the financial support for this research contributed by the National Key Research and Development Program of China (grant no. 2016YFC0600301), the Strategic Priority Research Program (B) of the Chinese Academy of Sciences (grant XDB03010700) and the National Natural Science Foundation of China (grant nos. 41804058, 41674064, 41522401, 41474068, 41574056).

## Appendix A. Supplementary material

Supplementary material related to this article can be found online at <https://doi.org/10.1016/j.epsl.2019.02.037>.

## References

- Alsina, D., Snieder, R., 1995. Small-scale sublithospheric continental mantle deformation – constraints from SKS splitting observations. *Geophys. J. Int.* 123, 431–448.
- Bowman, J.R., Ando, M., 1987. Shear-wave splitting in the upper-mantle wedge above the Tonga subduction zone. *Geophys. J. R. Astron. Soc.* 88, 25–41.
- Chen, W.-P., Martin, M., Tseng, T.-L., Nowack, R.L., Hung, S.-H., Huang, B.-S., 2010. Shear-wave birefringence and current configuration of converging lithosphere under Tibet. *Earth Planet. Sci. Lett.* 295, 297–304.
- Chen, W.-P., Ozalaybey, S., 1998. Correlation between seismic anisotropy and Bouguer gravity anomalies in Tibet and its implications for lithospheric structures. *Geophys. J. Int.* 135, 93–101.
- Chen, Y., Li, W., Yuan, X., Badal, J., Teng, J., 2015. Tearing of the Indian lithospheric slab beneath southern Tibet revealed by SKS-wave splitting measurements. *Earth Planet. Sci. Lett.* 413, 13–24.
- Clark, M.K., Royden, L.H., 2000. Topographic ooze: building the eastern margin of Tibet by lower crustal flow. *Geology* 28, 703–706.
- Crampin, S., Peacock, S., 2005. A review of shear-wave splitting in the compliant crack-critical anisotropic Earth. *Wave Motion* 41 (1), 59–77.
- England, P., McKenzie, D., 1982. A thin viscous sheet model for continental deformation. *Geophys. J. R. Astron. Soc.* 70, 295–321.
- Fu, Y.V., Chen, Y.J., Li, A., Zhou, S., Liang, X., Ye, G., Jin, G., Jiang, M., Ning, J., 2008. Indian mantle corner flow at southern Tibet revealed by shear wave splitting measurements. *Geophys. Res. Lett.* 35 (2), L02308.
- Gao, S.S., Liu, K.H., Abdelsalam, M.G., 2010. Seismic anisotropy beneath the Afar Depression and adjacent areas: implications for mantle flow. *J. Geophys. Res.* 115, B12330.
- Hou, Z.Q., Zhao, Z.D.D., Gao, Y.F., Yang, Z.M., Jiang, W., 2006. Tearing and dischroal subduction of the Indian continental slab: evidence from Cenozoic Gangdese volcano-magmatic rocks in south Tibet. *Acta Petrol. Sin.* 22, 761–774.
- Huang, W.C., Ni, J.F., Tilmann, F., Nelson, D., Guo, J.R., Zhao, W.J., Mechie, J., Kind, R., Saul, J., Rapine, R., Hearn, T.M., 2000. Seismic polarization anisotropy beneath the central Tibetan Plateau. *J. Geophys. Res., Solid Earth* 105, 27979–27989.
- Kapp, P., DeCelles, P.G., Gehrels, G.E., Heizler, M., Ding, L., 2007. Geological records of the Lhasa-Qiangtang and Indo-Asian collisions in the Nima area of central Tibet. *Geol. Soc. Am. Bull.* 119, 917–932.
- Kapp, P., Murphy, M.A., Yin, A., Harrison, T.M., Ding, L., Guo, J.H., 2003. Mesozoic and Cenozoic tectonic evolution of the Shiquanhe area of western Tibet. *Tectonics* 22 (4), 1029.
- Kapp, P., Yin, A., Harrison, T.M., Ding, L., 2005. Cretaceous-Tertiary shortening, basin development, and volcanism in central Tibet. *Geol. Soc. Am. Bull.* 117, 865–878.
- Kapp, P., Yin, A., Manning, C.E., Murphy, M., Harrison, T.M., Spurlin, M., Lin, D., Deng, X.G., Wu, C.M., 2000. Blueschist-bearing metamorphic core complexes in the Qiangtang block reveal deep crustal structure of northern Tibet. *Geology* 28, 19–22.
- Kind, R., Yuan, X., 2010. Seismic images of the biggest crash on Earth. *Science* 329, 1479–1480.
- Kremer, C., Blewitt, G., Klein, E.C., 2014. A geodetic plate motion and Global Strain Rate Model. *Geochem. Geophys. Geosyst.* 15, 3849–3889.
- Kumar, M.R., Singh, A., 2008. Evidence for plate motion related strain in the Indian shield from shear wave splitting measurements. *J. Geophys. Res., Solid Earth* 113, B08306.
- Li, C., Van der Hilst, R.D., Meltzer, A.S., Engdahl, E.R., 2008. Subduction of the Indian lithosphere beneath the Tibetan Plateau and Burma. *Earth Planet. Sci. Lett.* 274, 157–168.
- Li, Y., Wu, Q., Pan, J., Zhang, F., Yu, D., 2013. An upper-mantle S-wave velocity model for East Asia from Rayleigh wave tomography. *Earth Planet. Sci. Lett.* 377, 367–377.

- Liang, C., Song, X., 2006. A low velocity belt beneath northern and eastern Tibetan Plateau from Pn tomography. *Geophys. Res. Lett.* 33, L22306.
- Liang, X., Chen, Y., Tian, X., Chen, Y.J., Ni, J., Gallegos, A., Klempere, S.L., Wang, M., Xu, T., Sung, C., Si, S., Lan, H., Teng, J., 2016a. 3D imaging of subducting and fragmenting Indian continental lithosphere beneath southern and central Tibet using body-wave finite-frequency tomography. *Earth Planet. Sci. Lett.* 443, 162–175.
- Liang, X., Tian, X., Zhu, G., Wu, C., Duan, Y., Li, W., Zhou, B., Zhang, M., Yu, G., Nie, S., Wang, G., Wang, M., Wu, Z., Liu, Z., Guo, X., Zhou, X., Wei, Z., Xu, T., Zhang, X., Bai, Z., Chen, Y., Teng, J., 2016b. SANDWICH: a 2D broadband seismic array in central Tibet. *Seismol. Res. Lett.* 87, 864–873.
- Liu, H., Niu, F., 2012. Estimating crustal seismic anisotropy with a joint analysis of radial and transverse receiver function data. *Geophys. J. Int.* 188, 144–164.
- Liu, K.H., Gao, S.S., 2011. Estimation of the depth of anisotropy using spatial coherency of shear-wave splitting parameters. *Bull. Seismol. Soc. Am.* 101, 2153–2161.
- McNamara, D.E., Owens, T.J., Silver, P.G., Wu, F.T., 1994. Shear-wave anisotropy beneath the Tibetan Plateau. *J. Geophys. Res., Solid Earth* 99, 13655–13665.
- Rapine, R., Tilmann, F., West, M., Ni, J., Rodgers, A., 2003. Crustal structure of northern and southern Tibet from surface wave dispersion analysis. *J. Geophys. Res., Solid Earth* 108.
- Sandvol, E., Ni, J., Kind, R., Zhao, W.J., 1997. Seismic anisotropy beneath the southern Himalayas-Tibet collision zone. *J. Geophys. Res., Solid Earth* 102, 17813–17823.
- Savage, M.K., 1999. Seismic anisotropy and mantle deformation: what have we learned from shear wave splitting? *Rev. Geophys.* 37, 65–106.
- Sherrington, H.F., Zandt, G., Frederiksen, A., 2004. Crustal fabric in the Tibetan Plateau based on waveform inversions for seismic anisotropy parameters. *J. Geophys. Res., Solid Earth* 109, B02312.
- Silver, P.G., 1996. Seismic anisotropy beneath the continents: probing the depths of geology. *Annu. Rev. Earth Planet. Sci.* 24, 385–432.
- Silver, P.G., Chan, W.W., 1991. Shear-wave splitting and subcontinental mantle deformation. *J. Geophys. Res., Solid Earth* 96, 16429–16454.
- Solon, K.D., Jones, A.G., Nelson, K.D., Unsworth, M.J., Kidd, W.F., Wei, W., Tan, H., Jin, S., Deng, M., Booker, J.R., Li, S., Bedrosian, P., 2005. Structure of the crust in the vicinity of the Bangong-Nujiang suture in central Tibet from INDEPTH magnetotelluric data. *J. Geophys. Res., Solid Earth* 110, 1–20.
- Tapponnier, P., Xu, Z.Q., Roger, F., Meyer, B., Arnaud, N., Wittlinger, G., Yang, J.S., 2001. Geology – oblique stepwise rise and growth of the Tibet plateau. *Science* 294, 1671–1677.
- Tatham, D.J., Lloyd, G.E., Butler, R.W.H., Casey, M., 2008. Amphibole and lower crustal seismic properties. *Earth Planet. Sci. Lett.* 267, 118–128.
- Taylor, M., Yin, A., 2009. Active structures of the Himalayan-Tibetan orogen and their relationships to earthquake distribution, contemporary strain field, and Cenozoic volcanism. *Geosphere* 5, 199–214.
- Taylor, M., Yin, A., Ryerson, F.J., Kapp, P., Ding, L., 2003. Conjugate strike-slip faulting along the Bangong-Nujiang suture zone accommodates coeval east-west extension and north-south shortening in the interior of the Tibetan Plateau. *Tectonics* 22 (4), 1044.
- Tian, X., Chen, Y., Tseng, T.-L., Klempere, S.L., Thybo, H., Liu, Z., Xu, T., Liang, X., Bai, Z., Zhang, X., Si, S., Sun, C., Lan, H., Wang, E., Teng, J., 2015. Weakly coupled lithospheric extension in southern Tibet. *Earth Planet. Sci. Lett.* 430, 171–177.
- Wu, J., Zhang, Z., Kong, F., Yang, B.B., Yu, Y., Liu, K.H., Gao, S.S., 2015. Complex seismic anisotropy beneath western Tibet and its geodynamic implications. *Earth Planet. Sci. Lett.* 413, 167–175.
- Wüstefeld, A., Bokelmann, G., 2007. Null detection in shear-wave splitting measurements. *Bull. Seismol. Soc. Am.* 97, 1204–1211.
- Wüstefeld, A., Bokelmann, G., Zaroli, C., Barruol, G., 2008. SplitLab: a shear-wave splitting environment in Matlab. *Comput. Geosci.* 34, 515–528.
- Xue, M., Allen, R.M., 2005. Asthenospheric channeling of the Icelandic upwelling: evidence from seismic anisotropy. *Earth Planet. Sci. Lett.* 235, 167–182.
- Yin, A., 2000. Mode of Cenozoic east-west extension in Tibet suggesting a common origin of rifts in Asia during the Indo-Asian collision. *J. Geophys. Res., Solid Earth* 105, 21745–21759.
- Yin, A., 2010. Cenozoic tectonic evolution of Asia: a preliminary synthesis. *Tectonophysics* 488, 293–325.
- Yin, A., Harrison, T.M., 2000. Geologic evolution of the Himalayan-Tibetan orogen. *Annu. Rev. Earth Planet. Sci.* 28, 211–280.
- Yin, A., Taylor, M.H., 2011. Mechanics of V-shaped conjugate strike-slip faults and the corresponding continuum mode of continental deformation. *Geol. Soc. Am. Bull.* 123, 1798–1821.
- Zhang, S.Q., Karato, S., 1995. Lattice preferred orientation of olivine aggregates deformed in simple shear. *Nature* 375, 774–777.
- Zhang, X., Teng, J., Sun, R., Romanelli, F., Zhang, Z., Panza, G.F., 2014. Structural model of the lithosphere-asthenosphere system beneath the Qinghai-Tibet Plateau and its adjacent areas. *Tectonophysics* 634, 208–226.
- Zhao, J., Murodov, D., Huang, Y., Sun, Y., Pei, S., Liu, H., Zhang, H., Fu, Y., Wang, W., Cheng, H., Tang, W., 2014. Upper mantle deformation beneath central-southern Tibet revealed by shear wave splitting measurements. *Tectonophysics* 627, 135–140.
- Zhao, J., Yuan, X., Liu, H., Kumar, P., Pei, S., Kind, R., Zhang, Z., Teng, J., Ding, L., Gao, X., Xu, Q., Wang, W., 2010. The boundary between the Indian and Asian tectonic plates below Tibet. *Proc. Natl. Acad. Sci. USA* 107, 11229–11233.
- Zhao, L.F., Xie, X.B., He, J.K., Tian, X.B., Yao, Z.X., 2013. Crustal flow pattern beneath the Tibetan Plateau constrained by regional Lg-wave Q tomography. *Earth Planet. Sci. Lett.* 383, 113–122.
- Zhu, G., Liang, X., Tian, X., Yang, H., Wu, C., Duan, Y., Li, W., Zhou, B., 2017. Analysis of the seismicity in central Tibet based on the SANDWICH network and its tectonic implications. *Tectonophysics* 702, 1–7.